catalysts

MDPI

Article

Photocatalytic Activity and Reusability of F, Sm^{3+} Co-Doped TiO_2/MWCNTs Hybrid Heterostructure for Efficient Photocatalytic Degradation of Brilliant Black Bis-Azo Dye

Sabastian Simbarashe Mukonza [1], Nhamo Chaukura [2] and Ajay Kumar Mishra [3,4,5,*]

[1] Department of Civil Engineering, National Pingtung University of Science & Technology, Pingtung 91201, Taiwan
[2] Department of Physical and Earth Sciences, Sol Plaatje University, Kimberley 8301, South Africa
[3] College of Medicine and Chemical Engineering, Hebei University of Science and Technology, Shijiazhuang 050018, China
[4] Academy of Nanotechnology and Waste Water Innovations, Johannesburg 2007, South Africa
[5] Department of Chemistry, Durban University of Technology, Steve Biko Road, Durban 4001, South Africa
* Correspondence: ajaykmishraedu@gmail.com

Abstract: A global freshwater pollution catastrophe is looming due to pollutants of emerging concern (PECs). Conventional water treatment methods are limited in removing PECs such as pharmaceuticals and dye house effluent from aquatic systems. This study provides an effective potential solution by developing an innovative wastewater treatment method based on solar-light-responsive semiconductor-based photocatalysts. A sol-gel synthesis technique was used to produce Fluorine-Sm^{3+} co-doped TiO_2 (0.6% Sm^{3+}) (FST3) photocatalysts. This was followed by loading multi-walled carbon nanotubes (MWCNTs) in the range of 0.25 to 1 wt% into the FST3 matrix. Solid state UV-visible spectroscopy measurements showed a bathochromic shift into the visible light region after the co-doping of TiO_2, whereas XRD analysis confirmed the presence of predominantly anatase polymorphs of TiO_2. The FT-IR and EDX results confirmed the presence of the F and Sm^{3+} dopants in the synthesised photocatalysts. XRD and TEM measurements confirmed that the crystallite sizes of all synthesised photocatalysts ranged from 12–19 nm. The resultant photocatalysts were evaluated for photocatalytic degradation of Brilliant Black BN bis-azo dye in aqueous solution under simulated solar irradiation. FST3 completely degraded the dye after 3 h, with a high apparent rate constant (K_a) value (2.73×10^{-2} min^{-1}). The degree of mineralisation was evaluated using the total organic carbon (TOC) technique, which revealed high TOC removal (82%) after 3 h and complete TOC removal after 4 h. The incorporation of F improved the optical properties and the surface chemistry of TiO_2, whereas Sm^{3+} improved the quantum efficiency and the optical properties. These synergistic effects led to significantly improved photocatalytic efficiency. Furthermore, incorporating MWCNTs into the F and Sm^{3+} co-doped TiO_2 (0.6% Sm^{3+}) improved the reaction kinetics of the FST3, effectively reducing the reaction time by over 30%. Recyclability studies showed that after 5 cycles of use, the FST3/C1 degradation efficiency dropped by 7.1%, whereas TiO_2 degradation efficiency dropped by 33.4% after the same number of cycles. Overall, this work demonstrates a sustainable and efficient dye-removal technique.

Keywords: bis-azo dye; photocatalysis; photo-mineralisation; synergistic effects; TiO_2

check for updates

Citation: Mukonza, S.S.; Chaukura, N.; Mishra, A.K. Photocatalytic Activity and Reusability of F, Sm^{3+} Co-Doped TiO_2/MWCNTs Hybrid Heterostructure for Efficient Photocatalytic Degradation of Brilliant Black Bis-Azo Dye. *Catalysts* **2023**, *13*, 86. https://doi.org/10.3390/catal13010086

Academic Editors: Rosanna Pagano, Ludovico Valli and Zois Syrgiannis

Received: 2 December 2022
Revised: 27 December 2022
Accepted: 29 December 2022
Published: 31 December 2022

Copyright: © 2022 by the authors. Licensee MDPI, Basel, Switzerland. This article is an open access article distributed under the terms and conditions of the Creative Commons Attribution (CC BY) license (https://creativecommons.org/licenses/by/4.0/).

1. Introduction

There is an increase in the levels of organic pollutants in ground and surface water emanating from the discharge of various organic industrial effluents into the environment. These organic pollutants include dye house effluent, pharmaceutical compounds, and agrochemicals [1]. When discharged into the environment, organic pollutants can bioaccumulate and bioconcentrate along the food chain, resulting in both acute and chronic

toxicity to animals and humans [2]. This is because they are resistant to self-decomposition and biodegradation in natural environments; thus, they are not efficiently eliminated by conventional water treatment methods that include flocculation, coagulation, membrane filtration, adsorption, and biodegradation [3].

Advanced oxidation processes (AOPs) have the capacity to mineralise recalcitrant organic pollutants into smaller, simpler, harmless molecules, such as CO_2 and H_2O [4,5]. TiO_2 semiconductor photocatalysis has proved to be a desirable AOP treatment method relative to other methods. TiO_2 is frequently used to photodegrade organic pollutants because it is relatively cheaper, non-toxic, and physically and chemically inert, and it has excellent electronic and optical properties. However, TiO_2 has high carrier-charge recombination and a high band-gap energy of 3.2 eV [6]. This means it is only responsive to UV radiation, limiting its applicability under solar radiation [7]. Another challenge with the use of the powdered form of TiO_2 is low photocatalyst recovery, due its high dispersibility in aqueous media [8]. In addition, TiO_2 on its own requires post-treatment filtration to recover the photocatalyst, thus complicating the treatment setup.

Accordingly, several doping strategies have been developed to mitigate against the drawbacks of TiO_2 photocatalysts. These include interstitial doping, where the dopant occupies an interstitial site in the TiO_2 lattice [9,10], and substitutional doping with various anions, in which the O^{2-} or Ti^{4+} vacancy in the TiO_2 matrix is substituted by a dopant [11]. Specifically, doping TiO_2 with F^- results in band gap reduction [11], shape and morphological control [12,13], bulk fluorination [14], and surface fluorination [15,16]. Furthermore, TiO_2 can be doped with different metal ions to manipulate its structure, electronic properties, and performance by modifying the properties. By acting as electron scavengers and increasing the interfacial charge transfer rate, metal dopants prevent electron charge-carrier recombination on the TiO_2 surface [17,18]. In addition, they induce the formation of Schottky barriers at the semiconductor and the metal dopant interface, resulting in reduced electron recombination on the surface with positive holes [17,18]. Metal dopants or the resulting structural defects may introduce new intraband-gap energy states, which are responsible for improved visible light activity, and they may also tune the redox potential of the photoexcited species to align with that of TiO_2 [17,18]. In the case of rare-earth metals, which have largely vacant f-orbitals with a tendency to complex with Lewis bases, they bond with functional groups of organic pollutants, concentrating the pollutant on the catalyst surface and thus enhancing surface adsorption [18,19]. Moreover, lanthanide photoluminescence properties of rare-earth-doped TiO_2 improve the activity of TiO_2 composites within the visible and near-infrared regions [20,21]. In this study, we used F^-, Sm^{3+} co-doping of TiO_2 to take advantage of all of the doping benefits.

Carbon nanotubes (CNTs) have shown different semiconducting, semimetallic and metallic characteristics due to their unique electronic properties. At different tube diameters and tube helicity, CNTs exhibit different electronic properties [22,23]. CNTs are good structural support materials on which TiO_2 can be anchored, providing high tensile strength, increased adsorption capacity, improved light responsiveness, and increased electron mobility properties [24]. The adsorption capacity of CNTs is demonstrated by high adsorption capacity for dioxins, fluorine, and cadmium [22,23]. Incorporating CNTs into the TiO_2 matrix to produce hybrid heterostructures has provided some insightful solutions to these challenges [25–27]. For instance, decorating the surfaces of CNTs with TiO_2 has resulted in enhanced photocatalytic performance in the photodegradation of organic pollutants [28,29].

When TiO_2 is coupled to CNT, there is an improvement in the photocatalytic degradation rate of dye through acting as electron sinks to eliminate or reduce generated carrier-charge recombination by trapping the photoexcited electrons from the TiO_2 conduction band (CB) into the CNT matrix [29]. In this role, CNTs can act as photosensitisers because they can absorb visible light and generate delocalised electrons that can be injected into the CB of TiO_2. Simultaneously, carbon atoms from the CNT structure can be a source of nonmetal dopants reducing the band gap of TiO_2 by creating mid-gap energy states

between the TiO_2 CB and valence band (VB) [23]. Immobilisation of TiO_2 on CNTs has been used to improve the photocatalyst recovery rate during photocatalysis while maintaining high dispersibility in solution [25,26]. This work focuses on analysing the effects of F, Sm^{3+} co-doping TiO_2/multiwalled carbon nanotube hybrid heterostructures for improved electronic and optical properties, improved quantum efficiency, and improved photocatalyst recovery.

The novelty and significance of this study stem from the use of a photocatalytic material with remarkable activity and reusability when exposed to solar light for the degradation of a uniquely stable and recalcitrant pollutant, BN bis-azo dye, in water. The designed photocatalyst is a promising material for two reasons: (1) it is an economical water treatment method that can be dependent on an environmentally friendly, freely available, and inexhaustible source of energy in the form of naturally harvested solar light from the sun, and (2) the high photostability of the photocatalyst demonstrated after several cycles of use means that the risk of secondary pollution through photocatalyst leaching into the treated water is minimized, and a longer photocatalyst life cycle demonstrates a cost-effective water-treatment process.

2. Results

2.1. Characteristics of MWCNT /F, Sm^{3+} Co-Doped TiO_2

2.1.1. Surface Functional Groups

Functional groups present on the sample surface can be interpreted from FTIR spectra (Figure 1a). In all the spectra there is a broad O-H stretch peak from 3200–3600 cm^{-1}, which is attributed to adsorption of moisture by the photocatalyst. The intensity of the TiO_2 O-H stretch peaks may thus signify the presence of high moisture content in the photocatalysts. The peaks at 1500 cm^{-1} signify the presence of -C-C- (stretch in ring), typical of the aromatic C-C- moieties of carbon nanotubes [30]. Around 1300 cm^{-1}, there is a less intense peak that might be attributed to the -C-O stretching mode due to the presence of oxidised CNTs, confirming successful functionalisation of multiwalled carbon nanotubes (MWCNTs). The peak at 850 cm^{-1} might be due to the presence of the -C-H bond in the hexagonal rings of carbon nanotubes. High intensity peaks symmetrical around 750 cm^{-1} in all spectra are ascribed to the Ti-O stretching and O-Ti-O bending modes [31–33].

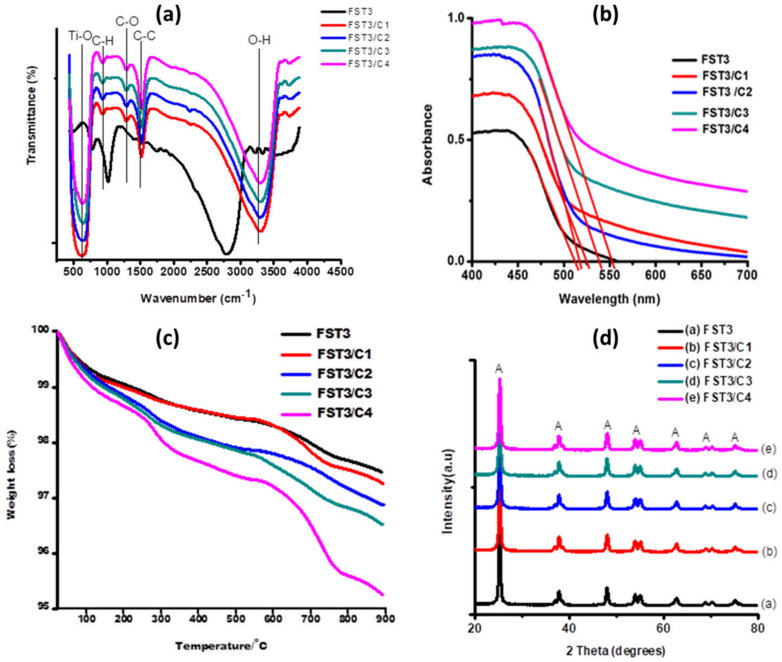


Figure 1. (**a**) FTIR spectra of different MWCNT loadings/F, Sm^{3+} co-doped TiO_2 (0.6% Sm^{3+}); (**b**) UV-Vis spectra for FST3/MWCNT with different MWCNT loadings used for direct approximation of

absorption wavelength. The red lines were used as extrapolation tangents for band-gap estimation; (**c**) TGA thermograms for FST3/MWCNT with different MWCNT loadings; and (**d**) XRD spectra for FST3/MWCNT with different MWCNT loadings.

2.1.2. Optical Properties

Optical properties of photocatalysts were measured using the UV-visible spectroscopy absorbance method. The absorption wavelength of each material is determined by directly drawing a tangent to the UV-vis absorption spectra of the sample (Figure 1b).

Optical properties show a considerable increase in the wavelength absorption edge of the F, Sm^{3+} co-doped TiO_2 (0.6% Sm^{3+}), with an increase in the MWCNTs load (Table 1). This increase in the absorption wavelength is due to the fact that MWCNTs absorb light in the visible light region, and furthermore, CNTs can act as precursors for C dopants, which in turn reduces the TiO_2 band gap [31,32]. Improved visible solar light absorption can also be ascribed to the synergistic effects of F, Sm^{3+} doping of TiO_2 and the incorporation of MWCNTs; this results in combined effects of light harvesting.

Table 1. Estimated absorption wavelengths and calculated band gaps for different MWCNT loadings.

Sample	Absorption Wavelength [nm]	Band Gap (E_g) [eV]
FST3	517	2.40
FST3/C1	525	2.36
FST3/C2	520	2.38
FST3/C3	540	2.29
FST3/C4	550	2.25

2.1.3. Thermal Properties

The TGA curves for FST3, FST3/C1, FST3/C2, FST3/C3, and FST3/C4 show different trends of weight loss over the same heating temperature range (Figure 1c). The order of thermal stability is as follows: FST3 > FST3/C1 > FST3/C2 > FST3/C3 > FST3/C4. For all the samples, weight loss of approximately 1% (100% to 99% in the heating temperature range of 20 °C to 100 °C) experienced by the samples could be attributed to loss of H_2O molecules in the form of moisture, H_2O of crystallisation in the TiO_2, and volatile organic residues from precursor molecules. Furthermore, a weight loss of approximately 1% experienced from 250 to 550 °C for all samples may be attributed to the loss of elementary dopants F and C (C liberated from MWCNTs). The onset of thermal degradation of oxidised MWCNTs starts at around 500 °C and degrades over a narrow temperature range. However, the various composites have different degradation onset temperatures. The 1% MWCNT composite starts to degrade at 550 °C, whereas 0.75% and 0.5% MWCNT composites start to degrade at 580 °C, and the degradation onset temperature of 0.25% and 0% MWCNT composites is further pushed to 630 °C. The general trend is that as the MWCNT loading on FST3 increased, there was a decrease in the thermal stability of the photocatalyst. The homogeneous distribution of thermally stable TiO_2 on the surface of MWCNTs also results in efficient and uniform heat transfer across the nanocomposite, thereby delaying the onset of decomposition. The different weight losses shown by both catalysts indicate that they are thermally stable over a temperature range of up to 250 °C and can be used under the same thermal conditions without undergoing thermal decomposition or losing dopant elements.

2.1.4. Crystallinity

The XRD analysis of FST3 with varied MWCNT compositions shows almost identical peaks (Figure 1d). The XRD patterns mainly show the anatase phase with a higher degree of crystallinity. The anatase TiO_2 peaks (labelled A in Figure 1d) were observed at 2θ positions

25.3°, 38.1°, 48.3°, 54.2°, 55.3°, 62.9°, and 75.4°, corresponding to the crystal planes of (101), (004), (200), (105), (211), (204), and (215), respectively [34]. The MWCNT fingerprint peaks occur at 2θ positions 26.0° and 43.4°, but all the composites did not reflect these MWCNT peaks because they are present in low concentrations. Moreover, the 26.0° peak might be overlapped by the broader shoulder of the anatase TiO_2 peak at 25.3°, since they are close to one another [35]. There are no visible Sm^{3+} peaks on all the spectra because Sm^{3+} is present in low quantities. Overall, there is a marginal increase in crystallite size as the MWCNT loading increases (Table 2). This can be attributed to agglomeration of both MWCNT and TiO_2 at higher MWCNT loading, which is also confirmed by TEM analysis (Figure 1c). When agglomeration occurs separately, there is phase separation of TiO_2 from MWCNT, which may result in an increase in average particulate size of TiO_2 as MWCNT loading increases. Increasing MWCNT resulted in low dispersibility of TiO_2 on MWCNT walls. Alternatively, at low MWCNT loading, the rate of hydrolysis and condensation reaction of TTIP is faster due to the limited number of carboxylate sites, resulting in the formation of relatively small TiO_2 particles [36].

Table 2. Crystallite size and lattice strain for different MWCNT loading on anatase TiO_2.

Sample	Crystallite Size (D) [nm]	Lattice Strain (η)
FST3	15.45	0.0107
FST3/C1	17.72	0.0093
FST3/C2	17.72	0.0093
FST3/C3	18.10	0.0091
FST3/C4	18.49	0.0089

2.1.5. Surface Morphology and Elemental Composition

The SEM micrograph shows the surface morphology of FST3/C1 containing low (0.25%) MWCNT loading (Figure 2a). The particles show a relatively high degree of agglomeration. The MWCNTs are not visible on the micrograph, possibly because of either their presence in small quantities, or they may be covered by TiO_2 particles. The complete wrapping of MWCNT by TiO_2 particles is appropriate for improving the photoactivity of the photocatalyst. Elemental composition shows the presence of Ti, C, O, F, Sm, and Si (Figure 2b). Fluorine and Sm^{3+} are present in small quantities, confirming the presence of the main dopants. The C confirms the presence of MWCNT, whereas the presence of Si may be due to contamination arising from borosilicate-based glassware.

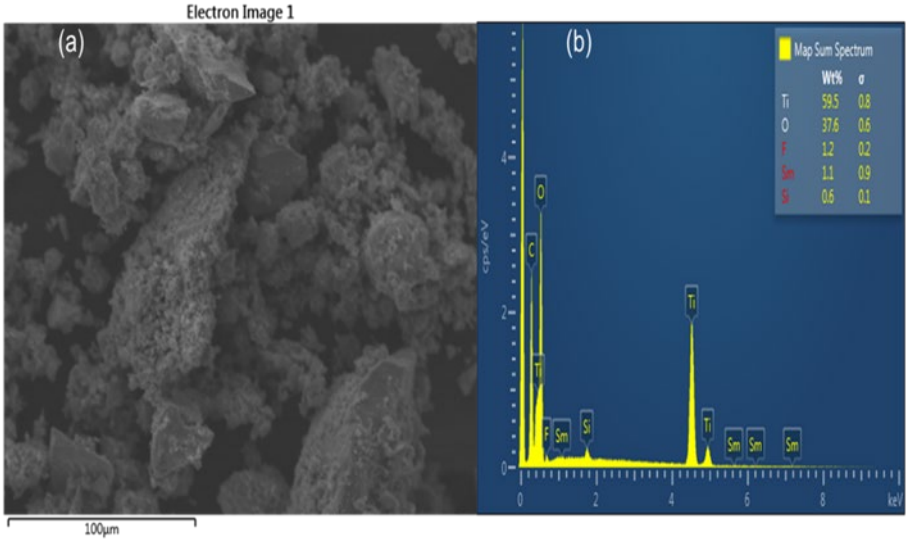


Figure 2. SEM/EDX images of FST3/C1: (**a**) SEM micrograph; and (**b**) EDX spectra.

2.1.6. Internal Morphology

The internal morphology of FST3/C1 may be attributed to the presence of MWCNTs and F, Sm^{3+} co-doped TiO_2 clusters (Figure 3a). Most of the CNTs are completely covered by F, Sm^{3+} co-doped TiO_2 matrices, whereas some isolated tubes remain uncovered. Bare MWCNTs are rod-like structures showing an off-whitish colour, and the homogeneous dispersion of F, Sm^{3+} co-doped TiO_2 on MWCNTs is confirmed by dark rods. Some of the MWCNTs are not uniformly decorated with TiO_2 clusters due to flaking-off of doped TiO_2 and loss of moisture during calcination at high temperatures. The selected area electron diffraction pattern of FST3/C1 (Figure 3b) shows the index of diffraction rings, confirming the presence of a crystalline TiO_2 anatase phase, a finding corroborated by XRD results [37]. The particle size distribution ranged from 15 to 20 nm, which is also confirmed by XRD crystallite size. This narrow size-distribution range reveals a relatively higher uniformity of doped TiO_2 particle sizes.

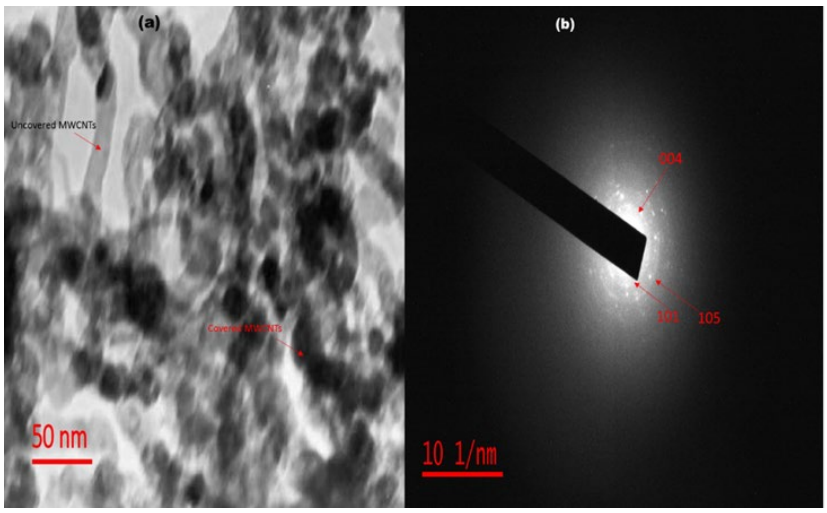


Figure 3. (**a**) TEM micrograph of FST3/C1; and (**b**) SAED diffraction ring patterns of FST3/C1.

2.1.7. Specific Surface Area

The specific surface area (SSA) of the photocatalysts was evaluated using the N_2 adsorption and desorption isotherm methods after degassing at 200 °C. The results showed that an increase in MWCNT loading was accompanied by an increased SSA of the co-doped TiO_2/MWCNT composite. This is because MWCNTs have a higher SSA. The SSA followed the order of MWCNT > FST3/C4 > FST3/C3 > FST3/C2 > FST3/C1 > FST3 (Table 3). Large SSA, which is good for a dispersing template, does not guarantee higher photocatalytic activity, as supported by the photocatalytic activity results. A previous study reported increased surface area for multi-doped TiO_2 on incorporating MWCNTs and further confirmed that this had an insignificant effect on the photocatalytic activity of the resulting composite [38].

Table 3. SSA for different MWCNT loading on F, Sm^{3+} co-doped TiO_2 sample.

Sample	SSA [m^2/g]
98% MWCNT *	216
FST3	19.4
FST3/C1	47.9
FST3/C2	50.7
FST3/C3	57.1
FST3/C4	61.8

* Data extracted from Sigma Aldrich certificate of conformance.

3. Discussion

3.1. Photodegradation Studies

The photodegradation of Brilliant Black BN azo dye under irradiation of simulated solar light was measured, and Figure 4a shows the Brilliant Black BN degradation rates by samples of different MWCNT loadings on F, Sm^{3+} co-doped TiO_2 (0.6% Sm^{3+}) (Figure 4a and actual values provided in Table 4). The general trend shows that the Brilliant Black BN degradation rates decreased with an increase in the MWCNT loading. The results showed the increase in degradation efficiency in the following order: FST3/C1 > FST3/C2 > FST3 > FST3/C3 > FST3/C4 (Figure 4a,b). This trend is explained by the fact that MWCNTs have both metallic and semimetallic properties, acting as semiconducting material with an optical absorption band in the visible light region [39]. The implication is that an increase in MWCNT loading results in increased optical absorption in the visible spectrum. This is confirmed by the UV-Vis data and approximated absorption wavelengths for various MWCNT loadings. In addition, MWCNTs can act as TiO_2 photosensitisers, injecting photoexcited electrons into the CB of TiO_2, or electron sinks, capturing photoexcited electrons from the CB to avoid carrier-charge recombination [40]. Doping TiO_2 with Sm^{3+} can also aid in concentrating the dye molecules on the surface of the photocatalyst and in increasing the adsorption of the dye. The electronic configuration of Sm^{3+} ([Xe] $4f^5$) implies there are vacant f-orbitals capable of forming dative bonds with the sulphonic, hydroxyl, and aminated groups of the dye molecules [19]. Therefore, all of these effects result in increased removal rates on incorporating MWCNT into the TiO_2 matrix [41]. However, an excessive increase in MWCNT results in diminishing the photocatalytic degradation rate. This may be attributed to aggregation and phase separation of both TiO_2 and MWCNT, which lead to nonuniform dispersion of TiO_2 on the MWCNT walls. An increase in MWCNTs results in agglomeration, which in turn decreases the active sites for photocatalysis [42].

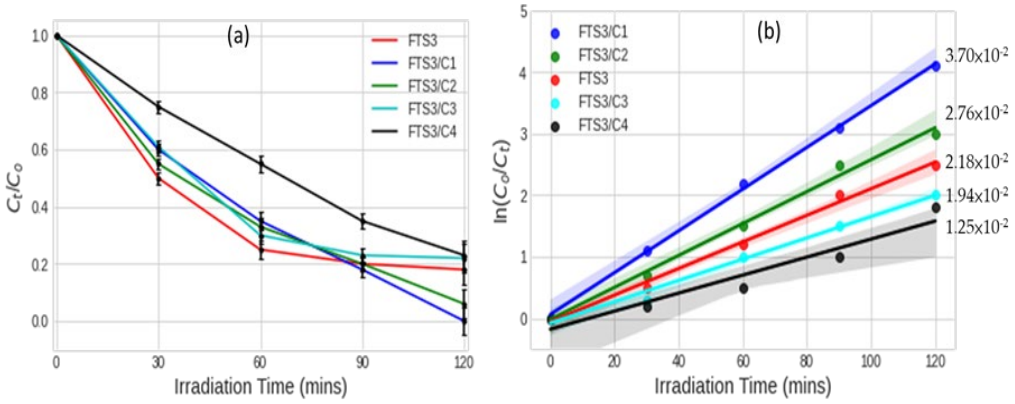


Figure 4. (**a**) Brilliant Black BN degradation rates for different MWCNT loadings on F, Sm^{3+} co-doped TiO_2 (0.6% Sm^{3+}) line plots with error bars; and (**b**) pseudo-first-order rate constants for degradation of Brilliant Black BN using photocatalysts with different MWCNT loadings on F, Sm^{3+} co-doped TiO_2 prediction lines with 95% confidence intervals.

Table 4. Degradation rates and rate constants for different MWCNT loadings on F, Sm^{3+} co-doped TiO_2 after 2 h of solar irradiation.

Sample	Degradation Rate after 120 min [%]	Rate Constant (K_a) [min^{-1}]
FST3	93.1	2.18×10^{-2}
FST3/C1	100.0	3.70×10^{-2}
FST3/C2	98.5	2.76×10^{-2}
FST3/C3	91.9	1.94×10^{-2}
FST4/C4	79.0	1.25×10^{-2}

Optimisation of CNT loading on TiO_2 photocatalyst for removal of organic pollutants is widely reported in the literature. For example, a previous study reported a comparative analysis of two different synthesis methods and found that the solvothermal synthesis method produced uniformly dispersed nanocrystals on MWCNTs compared to those produced by a sol-gel method [43]. The resultant photocatalytic activities showed that the morphological structure of TiO_2/MWCNTs impacts the rate of degradation of organic pollutants. Sol-gel synthesised MWCNT/TiO_2 (20% MWCNT) showed higher photocatalytic degradation of methylene blue (MB) than pure TiO_2. However, MWCNT/TiO_2 (20% MWCNT) synthesised through a solvothermal method showed higher photocatalytic activity during degradation of MB relative to MWCNT/TiO_2 synthesised by a sol-gel method [43]. The superior photoactivity of the solvothermal synthesised MWCNT/TiO_2 over the sol-gel-synthesised composite was attributed to the uniform distribution of TiO_2 particles on the MWCNT surface and a higher SSA. In another study, Hamadanian et al. [44] synthesised PbS/MWCNT and TiO_2/MWCNT by a simple wet process for the photocatalytic degradation of methyl orange. Degradation rates during the photocatalysis were 100 and 61.42% for TiO_2/MWCNT and PbS/MWCNT, respectively, after 30 min of visible light irradiation [44,45].

The correlation coefficient of the two results (degradation rate after 120 min and rate constant) shows a strong relationship (R^2 = 0.8137). Thus, both results confirm pseudo-first-order kinetics.

The reaction kinetics of the present study were compared to previous studies that used similar experiments to determine photocatalyst efficiency [31,36,38,46] (Table 5). Kuvarega et al. used solar light irradiation to degrade an initial concentration of 100 mgL^{-1} EY using an N, Pd^{3+}-TiO_2-MWCNT photocatalyst and obtained the highest K_a of all the experiments compared [36]. Despite using a higher initial concentration (50 mgL^{-1}) than other experiments (20 mgL^{-1}) [31,38,46], the photocatalyst in the present study performed better. The underlying reason for this could be that whereas this study used solar light, which has a broader spectrum that includes UV, visible, and NIR wavelengths, other studies used visible light as a light source. The difference in chemical structures of the target dyes may also be a contributing factor in the variation in photocatalytic performances of the different photocatalysts.

Table 5. Comparing the photocatalytic results in our study with other non-metal, metal multi-doped TiO2-MWCNT heterostuctures for photocatalytic activity enhancement.

Sample	Target Dye Pollutant	Initial Concentration [mg/L]	Source of Light	PC K_{app} [min^{-1}]	Ref
N,S-Nd^{3+}-TiO_2-MWCNT	Eosin blue shade	20	Visible	1.4×10^{-2}	[31]
N,S-Nd^{3+}-TiO_2-MWCNT	Eriochrome Black T	20	Visible	8.0×10^{-3}	[31]
N, Pd^{3+}-TiO_2-MWCNT	Eosin Yellow	100	Solar	3.42×10^{-2}	[36]
N, Pd^{3+}-TiO_2-MWCNT	Eosin Yellow	100	Visible	5.18×10^{-3}	[36]
N,S-Nd^{3+}-TiO_2-SWCNT	Eosin blue shade	20	Visible	1.5×10^{-2}	[38]
N,S-Nd^{3+}-TiO_2-MWCNT	Naphthol blue black	20	Visible	1.33×10^{-2}	[46]
F, Sm^{3+}-TiO_2-MWCNT	Brilliant Black BN	50	Solar	2.73×10^{-2}	Our study

To understand the degradation mechanism of Brilliant Black BN, the chemical structure must first be understood. Brilliant Black BN is a bis-azo-colored organic molecule (Figure 5), with extensive use in food, textile dying, drug manufacturing, and metal spraying in the automobile industries. As a result, its widespread use causes issues such as low water visibility, which leads to aquatic ecological challenges [47]. The presence of two azo groups in dye prompts an allergic reaction in people with salicylate intolerance. In addition to being a histamine liberator with a tendency to amplify the symptoms of asthma, its combination with benzoates has adverse health effects in children, leading to hyperactivity.

There are sufficient grounds for suspicion that bacteria in intestines can decompose these compounds into much more dangerous metabolites [48]. Thus, it is of great significance to this study to investigate an effective way to treat Brilliant-Black-BN-polluted wastewater.

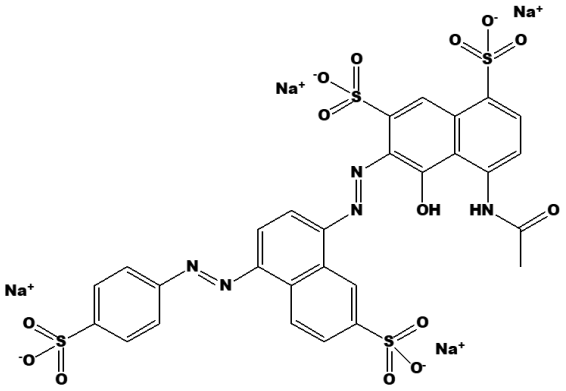


Figure 5. Chemical structure of Brilliant Black BN.

When solar light is irradiated on the sample, it interacts with the solid FST3/C1 in aqueous solution to break down Brilliant Black BN into smaller and simpler molecules through free radical attack (Figure 6). The final products of complete photodegradation are inorganic ions, CO_2, and H_2O, which are non-toxic. The MWCNTs decorated with F, Sm^{3+} co-doped TiO_2 are responsive to solar light; when these MWCNTs are radiated with visible light, their electrons undergo photoexcitation. The photoexcited electrons of the MWCNTs are in turn injected into the TiO_2 CB simultaneously, leaving a positive hole in the VB [49–51]. At the photocatalyst/aqueous solution interface, the photogenerated electrons in the CB attack the O_2 molecules to produce superoxide radicals ($\cdot O_2$) [45]. Due to the generation of electrons and positive holes, oxidation-reduction reactions take place at the surface of semiconductors. In the oxidative reaction, the positive holes react with the moisture (H_2O molecules) on the surface and produce hydroxyl radicals. Moisture causes the formation of a dense layer of hydroxyl groups on the photocatalyst surface, which improves photocatalyst dispersibility in water and promotes the formation of hydroxyl radicals. This can activate dye sensitization, because the intensity of the TiO_2 O-H stretch peaks in the FTIR spectra indicate the presence of high moisture content in the photocatalysts. Overall, this improves the photocatalyst performance [52].

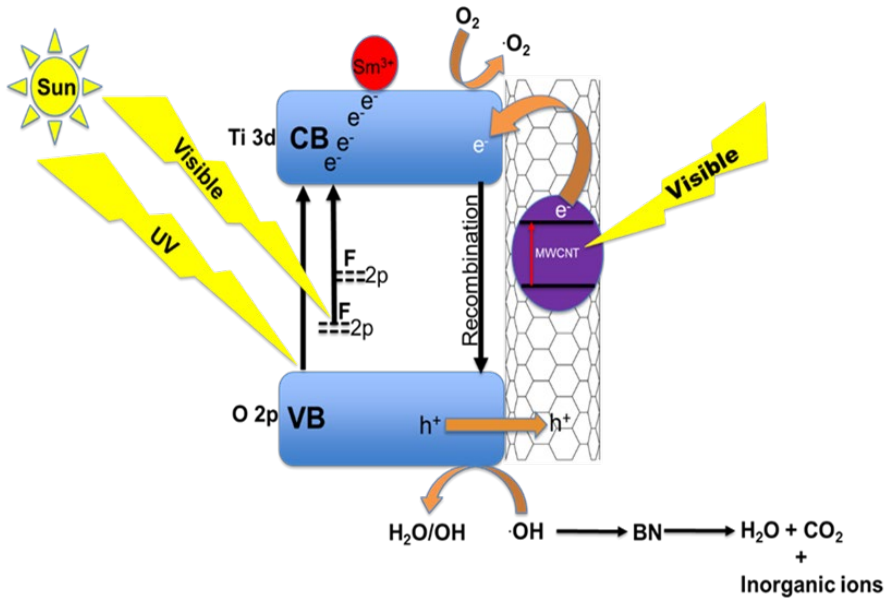


Figure 6. Proposed synergistic effects of F and Sm^{3+} doping on TiO_2-MWCNT hybrid structures.

Oxidative and reductive reactions are possible due to the catalytic effect. The dye molecule is broken down into simpler molecules by ·OH radicals generated during the TiO_2/UV photocatalytic process. The presence of Sm^{3+} and MWCNT results in improved quantum efficiency of TiO_2 because MWCNT and Sm^{3+} act as electron capture centres for reduced carrier-charge recombinations. Introduction of F dopant into the TiO_2 matrix and incorporation of MWCNT enhance the visible light absorption by band-gap reduction and the cumulative visible light absorption ability due to the intrinsic ability of MWCNTs. Colloidal quantum dots also provide an insightful understanding into the photocatalytic performances of F and Sm^{3+} doping on TiO_2/MWCNT hybrid structures due to their photoluminescence properties. Furthermore, their optoelectronic, electrical, and quantum properties are tuneable [53]. This makes use of colloidal quantum dots useful in optoelectronics and quantum photochemistry.

3.2. Reusability of the Photocatalyst

The photochemical stability of FST3/C1 during photocatalysis of Brilliant Black BN was evaluated by recycling the same catalyst for five cycles, whereas the photocatalytic degradation rate of the catalyst was measured after each cycle. Comparing the performance of FST3/C1 to that of pristine TiO_2 showed significant stability after five cycles, with the dye degradation rate decreasing from 99.8% in the first cycle to 92.7% in the fifth cycle (Figure 7a). This 7.1-percentage-point drop can be attributed to the 9-percentage- point mass loss of the photocatalyst (Table 6). For pristine TiO_2, the degradation rate dropped from 64.6% in the 1st cycle to 31.2% in the fifth cycle, a 33.4 percentage point drop in degradation efficiency. This can be attributed to the 39.2% loss of photocatalyst (Table 6). For both photocatalysts, there is a correlation between the drop in photocatalytic degradation and photocatalyst mass loss during photocatalyst recovery. Titania has low recoverability relative to the FSTiO_2/C1 hybrid photocatalyst because pristine TiO_2 is highly dispersible in aqueous solution, whereas immobilisation of TiO_2 nanoparticles on MWCNTs improves the recoverability of the photocatalyst without compromising the dispersibility.

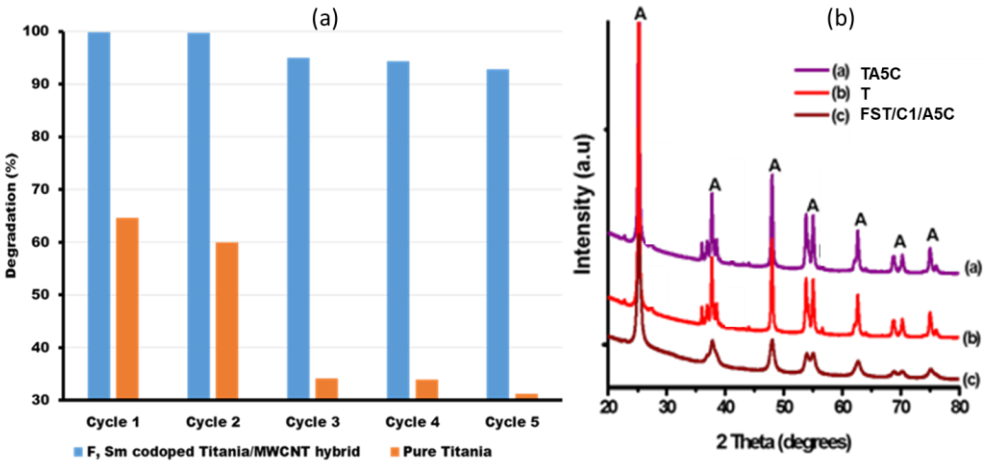


Figure 7. (**a**) Reusability/ recycling experiments for F, Sm^{3+} co-doped TiO_2/MWCNT and pure TiO_2 photocatalysts, and (**b**) XRD spectra for F, Sm^{3+} Co-doped-TiO_2/MWCNTs composites after photocatalytic reaction to check the stability of the catalyst.

Table 6. Photocatalyst recovery after five cycles of use.

Sample	Initial Mass [g]	Final Mass [g]	Recovery [%]
T	0.102	0.062	60.8
FST3/C1	0.1	0.91	91

XRD analysis was used to examine the stability of the catalysts' crystal structure for pristine TiO_2 and co-doped TiO_2/MWCNTs composite before and after the five cycle exper-

iments. The XRD spectra results for pristine TiO_2 before photocatalysis (T), pristine TiO_2 after five cycle use (TA5C), composite catalyst F, Sm^{3+} co-doped-TiO_2/MWCNTs before use (FST3/C1)—already shown in Figure 1d—and composite catalyst F, Sm^{3+} co-doped-TiO_2/MWCNTs post-photocatalysis (FST3/C1/A5C) are shown in Figure 7b. The results indicate that the crystal structure of all the photocatalysts did not change significantly after the fifth cycle, with only a marginal decrease in the XRD peak intensity detected for the two used photocatalysts (TA5C and FST3/C1/A5C) (Figure 7b). In this regard, all the catalysts can be classified as photostable, as reported in a similar study [54]. All the photocatalysts maintained stable anatase TiO_2 polymorphs shown by their sharp peaks labelled A (Figure 7b).

3.3. Total Organic Carbon

There is a possibility of producing intermediate products such as nitrated polyaromatic compounds, which are known to be toxic, mutagenic, teratogenic, and carcinogenic [55]. Thus, monitoring total organic carbon (TOC) during dye degradation is critical for determining the degree of mineralisation, photodegradation products, and byproducts. Ideally, photodegradation of dyes should completely mineralise the dye molecules to simpler and nontoxic compounds such as CO_2, H_2O, and inorganic ions [38]. The TOC concentration was determined to be 15 mgL^{-1} at an initial concentration of 50 mgL^{-1} Brilliant Black BN. After three hours of irradiation, photodegradation of Brilliant Black BN with FST3/C1 resulted in TOC removal of 82% (Figure 8). This was a significantly higher proportion of TOC removal, but the residual TOC concentration of 2.7 mgL^{-1} was significantly higher than the maximum permissible limit of 0.05 mgL^{-1}. Continued degradation up to four hours irradiation resulted in complete TOC removal, demonstrating complete mineralisation. However, this needs to be confirmed and corroborated with data from techniques such as mass spectroscopy.

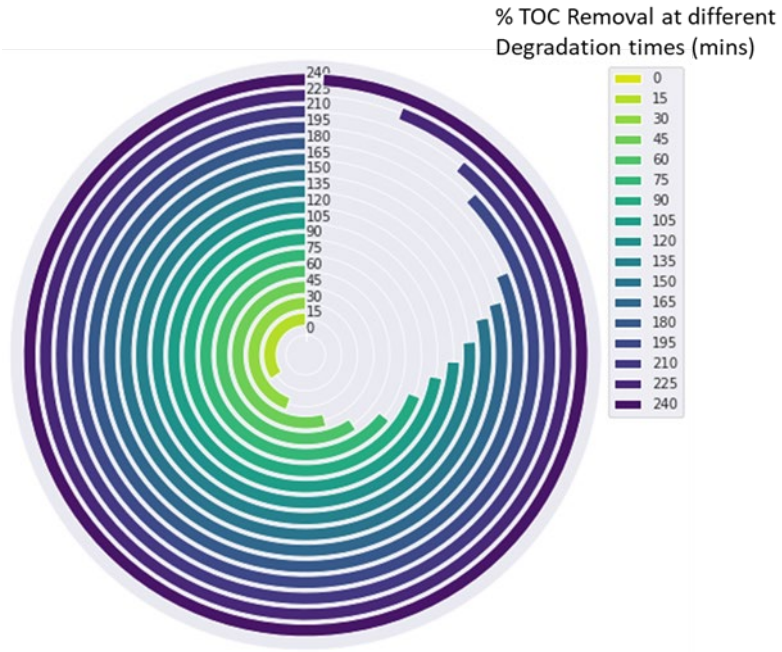


Figure 8. A circular bar chart depicting the removal of TOC with increasing degradation time.

4. Materials and Methods

4.1. Materials

Analytical reagent (AR) grades of titanium isopropoxide (TTIP) (97%), samarium nitrate hexahydrate ($Sm(NO_3)_3.6H_2O$) (99.9%), formic acid (90%), 2-propanol anhydrous (99.5%), multiwalled carbon nanotubes (MWCNTs) (purity > 99.5%), Brilliant Black BN (40%), ammonium fluoride (NH_4F) (98%), and concentrated HCl (32%) were supplied

by Sigma Aldrich, Taufkirchen, Germany and used without further treatment. Milli-Q deionised water (DI) was used throughout.

4.2. Functionalisation of MWCNTs

To introduce oxygen-carrying groups on the surface of MWCNTs, commercial MWCNTs (0.5 g) were added to a mixture of 2 mL 98% H_2SO_4 and 5.5 mL 70% HNO_3 and sonicated for 15 min, followed by continuous stirring for 6 h at 110 °C under reflux. The mixture was then cooled to room temperature and diluted with DI water (1 L) followed by filtration through a 0.2 µm Teflon filter under vacuum. The oxidized MWCNTs were dispersed into DI water (1 L) and further washed with acid until a pH of approximately 7 was reached.

4.3. Preparation MWCNT/F, Sm^{3+} Co-Doped TiO_2 (0.6% Sm^{3+})

The F, Sm^{3+} co-doped TiO_2/MWCNT photocatalyst was prepared using the one-pot sol-gel method (Figure 9). To 2-propanol (50 mL) was added an appropriate mass of MWCNTs, followed by sonication at 40 °C for 30 min. Thereafter, TTIP (10 mL) was added to the MWCNT solution, followed by further sonication for 30 min to form solution A. Samarium nitrate hexahydrate (46.4 mg) and NH_4F (510.2 mg) was dissolved in a mixture of 2-propanol (30 mL), formic acid (10 mL), DI water (10 mL) and HCl (3 mL) by continuously stirring for 30 min to make solution B. Solution B was added drop-wise to solution A and continuously stirred for 1 h until a white sol-gel was observed. The resultant sol-gel was aged for 24 h, followed by oven-drying overnight at 80 °C, after which the sample was calcined in a muffle furnace at 450 °C. The mass of $Sm(NO_3)_3.6H_2O$ weighed represented 0.6% Sm^{3+} dopant on TiO_2, whereas different proportions of MWCNT were weighed to give 0.25%, 0.5%, 0.75% and 1% MWCNT loadings (Table 7).

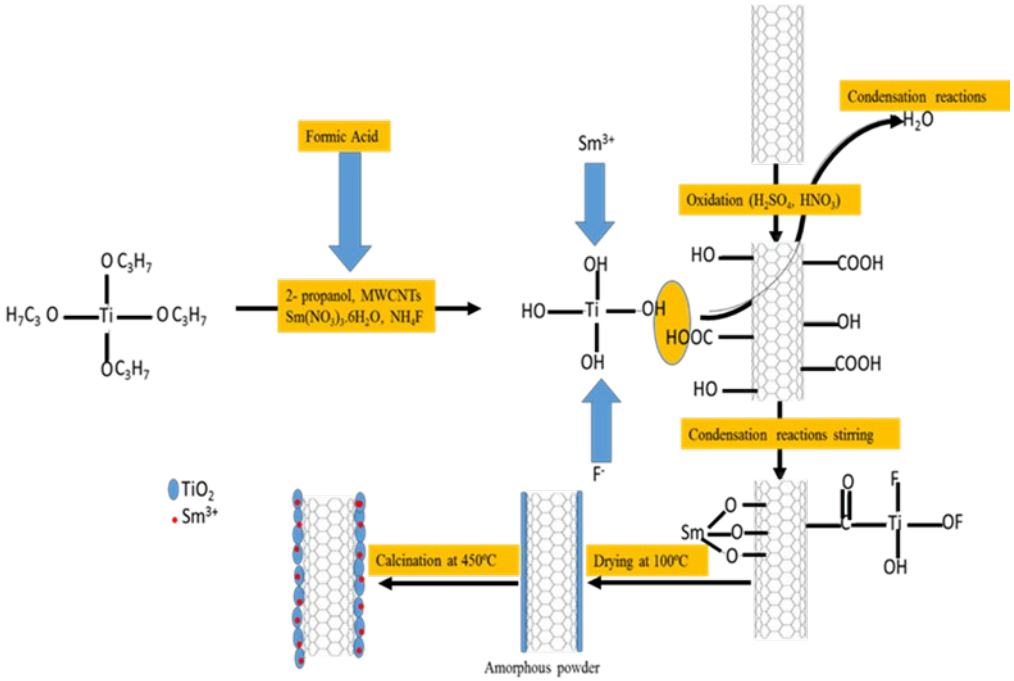


Figure 9. The synthesis route for F, Sm^{3+} co-doped TiO_2/MWCNTs using the sol-gel method.

4.4. Material Characterisation

4.4.1. Fourier Transform Infrared Spectroscopy and Raman Spectroscopy

The KBr disc method was used with the sample/KBr ratio of 1:20 to allow TiO_2-containing powders to be IR transparent. All FTIR analyses were performed using an FTIR spectrophotometer (Frontier, PerkinElmer, Midrand, South Africa). Raman spectra were collected on a Raman II FT-Raman module spectrometer coupled to a VERTEX 70

FT-IR spectrophotometer (Ettlingen, Germany), with 64 scans at a resolution of 4 cm^{-1} and scanning range of 20–700 cm^{-1} [56].

Table 7. Prepared photocatalysts and their notations.

Sample	Notation
Pristine TiO_2	T
F, Sm^{3+} co-doped TiO_2 (0.6% Sm^{3+})	FST3
F, Sm^{3+} co-doped TiO_2 (0.6% Sm^{3+})/0.25%MWCNT	FST3/C1
F, Sm^{3+} co-doped TiO_2 (0.6% Sm^{3+})/0.5%MWCNT	FST3/C2
F, Sm^{3+} co-doped TiO_2 (0.6% Sm^{3+})/0.75%MWCNT	FST3/C3
F, Sm^{3+} co-doped TiO_2 (0.6% Sm^{3+})/1%MWCNT	FST3/C4
Pristine TiO_2 after 5-cycle use	TA5C
F, Sm^{3+} co-doped TiO_2 (0.6% Sm^{3+})/0.25%MWCNT after 5-cycle use	FST3/C1/A5C

4.4.2. Ultraviolet-Visible Spectroscopy

The light response of the photocatalysts was recorded on a UV-Vis-NIR spectrometer (PerkinElmer, Midrand, South Africa Lambda 1050 UV-Visible-NIR) in the range of 200–800 nm using the 150 mm sphere-reflectance method. Deuterium and Tungsten lamps were used as UV and visible/NIR light sources, respectively. The operating parameters were a slit width of 4 mm and a photomultiplier response of 0.2 s, whereas $BaSO_4$ was used as a reflectance. The band gaps (E_g) of the semiconductor materials were calculated from the UV-Vis DRS spectrum (Equation (1)) [56].

$$E_g = \frac{hc}{\lambda} = \frac{1240}{\lambda} \quad (1)$$

where h is Planck's constant and c and λ are the speed and wavelength of light, respectively.

Kubelka–Munk (Equation (2)) is an absorption coefficient for predicting reflectance based on radiation transfer [30,31].

$$F(R) = \frac{(1-R)^2}{2R} \quad (2)$$

where $F(R)$ is the Kubelka–Munk function, and R is the percentage reflectance.

Tauc plots were used to estimate the band gaps for different photocatalysts. The optical quantities $F(R)$, hv, and E_g are related by Equation (3):

$$[F(R) \times hv]^{1/n} = A(hv - Eg)^n \quad (3)$$

where $F(R)$ is the Kubelka–Munk function, hv is the photon energy, E_g is the band-gap energy, n is the band gap under which electrons can undergo transition, and n can be $\frac{1}{2}$, 2, 3/2, or 3, corresponding to direct allowed transition, allowed indirect, forbidden direct, and forbidden indirect transitions, respectively.

4.4.3. Microscopy

The samples for microscopy analyses were prepared placing the powdered specimen on the adhesive carbon tape, which was then stuck to the sample holder and sputter-coated with 10–15 nm of graphite before being observed under the microscope. Scanning electron microscopy (SEM) analyses were performed on a JOEL IT 300 equipped with an Oxford energy-dispersive X-ray detector. Information on the elemental composition of the sample was obtained using a JOEL IT 300 with an Oxford EDX detector.

For transmission electron microscopy (TEM), samples were prepared by sonicating the samples in methanol for 10 min and small droplets of the suspension were then

deposited onto the lacy carbon-supported copper grids. The grids were allowed to dry before mounting the samples on the sample holder for TEM analysis. TEM analysis subsequently was performed using a JEOL JEM2100 transmission electron microscope (Tokyo, Japan).

4.4.4. Thermogravimetric Analysis

A thermogravimetric analyser (TGA) coupled to a differential scanning calorimetry (DSC) and TGA mode on a SDT Q600 (Selb, Germany) was used to investigate the thermal properties of different photocatalysts. Data analysis was performed through TA Universal analysis, software Q series Q600. Samples were analysed at a heating rate of 10 °C/min under N_2 (20 mL/min) over a temperature range of 20 to 900 °C.

4.4.5. X-ray Diffraction Analysis

Powdered samples were mounted onto a silica sample holder using a bracket sample stage. The powder X-ray diffraction of the sample was performed using a Rigaku SmartLab, Japan X-ray diffractometer using Cu Kα radiation source (λ= 1.5406 Å) in the wide-angle spectra range of 20–80°. The crystallite sizes (D) were determined using the Scherrer equation (Equation (4)).

$$D = \frac{K\lambda}{\beta Cos\theta} \tag{4}$$

where K is a dimensionless constant, 2θ is the diffraction angle, λ is the wavelength of the X-ray radiation, and β is the full width at half maximum (FWHM) of the diffraction peak [57–59].

4.4.6. Specific Surface Area

Specific surface area and porosity were measured using the TriStar II 3020, Selb, Germany. The analysis was carried out using the standard N_2 absorption method at a degassing temperature of 195 °C, the equilibration interval being 5 s, and no thermal correction was done.

4.5. Evaluation of Catalytic Activity

The photocatalytic activity of all samples was evaluated by measuring the photocatalytic degradation of Brilliant Black BN under solar light irradiation. For every sample, 100 mg of photocatalyst in 100 mL of 50 mg/L Brilliant Black BN was mixed and stirred in darkness for 1 h to attain absorption equilibrium before solar light irradiation. The pH of this solution was measured to be equal to 6.8. A solar simulator (HAL–320) supplied by ASAHI SPECTRAL, Japan was used to generate the required spectral irradiance for photocatalysis. The 300 W compact Xenon lamp was the light source, and a light intensity of 60% was used.

Aliquots of 4 mL were drawn using a 10 mL syringe and filtered through the GH Polypro membrane (GHP) syringe disc filter. Filtered samples were analysed for absorbance using the UV-visible spectrophotometer at a wavelength of 574.9 nm. A calibration curve was obtained using different concentrations ranging from (5–50 mg/L) and used to determine the concentration of the samples sampled at different sampling intervals. The concentration of Brilliant Black BN at time (t) was calculated using Equation (5) [59,60]:

$$\%BN\ Degradation = \frac{(C_0 - C_t)}{C_0} \times 100 \tag{5}$$

where C_o is the initial dye concentration, and C_t is dye concentration at time t.

4.6. Catalyst Reusability

To evaluate the reusability of both pure TiO_2 and F, Sm^{3+} co-doped TiO_2/MWCNTs photocatalysts, the photodegradation experiments were repeated 5 times using the same

recovered catalyst and freshly prepared 50 mg/L Brilliant Black BN dye solution. All the experimental conditions and parameters were kept constant. After every photodegradation cycle, the catalyst was rinsed with DI water to remove all organic contaminants that may lead to cross-contamination. The catalyst was recovered by vacuum filtration through a 0.2 µm Teflon filter and the performance was measured by evaluating the percentage degradation after every cycle. The photochemical stability of the photocatalysts was evaluated before and after each photodegradation cycle using XRD spectroscopy and SEM techniques [61,62].

5. Perspectives, Future Outlook and Prospective Studies

The photocatalytic effects and reusability of F, Sm^{3+} co-doped TiO_2/MWCNTs heterostructure in the degradation of BN bis-azo dye have been investigated in this study. The characterization was performed in detail, including the EDX elemental composition. However, there is a need to comprehend the various oxidation states of the various elements present in the photocatalyst using X-ray Photoelectron Spectroscopy (XPS) [63]. Additionally, the FTIR spectra indicate a dense network of hydroxyl groups on the photocatalyst surface, which needs to be confirmed by electron spin resonance (ESR) analysis. Although the optical properties of the photocatalyst are thoroughly discussed, there is a need to further relate the optical properties to the electronic structure of the designed photocatalyst, including band potential values, mid-gap-states energy levels, and the alignment of band potential levels with redox potential values of the various reactions occurring during the course of photomineralisation. This can be accomplished through the use of density functional theory (DFT), flat-band potential (Efb) by the Mott–Schottky (M-S) test, and electron paramagnetic resonance (EPR) [64,65]. The complete TOC removal needs to be followed up with molecular determination using mass spectrometry. All of these gaps are being combined as part of a consolidated plan for current and future work, which will be primarily focused on electrophotocatalysis.

6. Conclusions

A modified sol-gel synthesis method was successfully used to fabricate F, Sm^{3+} co-doped TiO_2/MWNCT hybrid photocatalyst principally consisting of anatase phase. The UV-Vis absorption spectra showed increased optical absorption properties with an increase in MWCNT loading. The crystallite sizes ranged from 15.4 to 18.4 nm, as confirmed by the XRD measurements. An excessive increase in MWCNT loading onto TiO_2 resulted in the reduction in photocatalytic activity, which might be ascribed to effects of agglomeration. The synergistic effects of incorporating different dopants F, Sm^{3+} and incorporation of MWCNT resulted in better photocatalytic activity relative to co-doped TiO_2, but further increases of MWCNT loading to above 0.5% (wt.%) resulted in significant reduction in photocatalytic activity. The FST3/C1 composite with the lowest percentage of MWCNT (0.25% loading) exhibited the maximum photocatalytic activity (complete degradation) after 2 h of irradiation. These findings confirm the unique properties of CNTs and their potential application in water treatment. A comparison of reusability between pure TiO_2 and FST3/C1 showed a 33.4% and 7% drop in photocatalytic activity, respectively, after 5 cycles of use, attributed to photocatalyst recovery after use. Overall, this is a promising method for the treatment of wastewater contaminated with azo dyes and has the potential to reduce both operating and disposal costs.

Author Contributions: Conceptualization, S.S.M. and A.K.M.; methodology, S.S.M.; software, N.C.; validation, N.C., S.S.M. and A.K.M.; formal analysis, S.S.M. and N.C.; investigation, S.S.M.; resources, A.K.M.; data curation, S.S.M. and N.C.; writing—original draft preparation, S.S.M.; writing—review and editing, N.C. and A.K.M.; visualization, S.S.M. and N.C.; supervision, A.K.M. and N.C.; project administration, A.K.M.; funding acquisition, A.K.M. All authors have read and agreed to the published version of the manuscript.

Funding: This research received no external funding.

Data Availability Statement: Anyone requesting data presented in this study can obtain it through the corresponding author.

Acknowledgments: The authors are grateful to the University of South Africa for access to laboratory facilities.

Conflicts of Interest: The authors declare no conflict of interest.

References

1. Pandis, P.K.; Kalogirou, C.; Kanellou, E.; Vaitsis, C.; Savvidou, M.G.; Sourkouni, G.; Zorpas, A.A.; Argirusis, C. Key Points of Advanced Oxidation Processes (AOPs) for Wastewater, Organic Pollutants and Pharmaceutical Waste Treatment: A Mini Review. *Chemengineering* **2022**, *6*, 8. [CrossRef]
2. Guo, W.; Pan, B.; Sakkiah, S.; Yavas, G.; Ge, W.; Zou, W.; Tong, W.; Hong, H. Persistent Organic Pollutants in Food: Contamination Sources, Health Effects and Detection Methods. *Int. J. Environ. Res. Public Health* **2019**, *16*, 4361. [CrossRef] [PubMed]
3. Babu, B.R.; Parande, A.K.; Raghu, S.; Kumar, T.P. Cotton textile processing: Waste generation and effluent treatment. *J. Cotton Sci.* **2007**, *11*, 141–153.
4. Kouvelis, K.; Kampioti, A.A.; Petala, A.; Frontistis, Z. Degradation of Sulfamethoxazole Using a Hybrid CuO_x–$BiVO_4$/SPS/Solar System. *Catalysts* **2022**, *12*, 882. [CrossRef]
5. Rekhate, C.V.; Srivastava, J.K. Recent advances in ozone-based advanced oxidation processes for treatment of wastewater- A review. *Chem. Eng. J. Adv.* **2020**, *3*, 100031. [CrossRef]
6. Luttrell, T.; Halpegamage, S.; Tao, J.; Kramer, A.; Sutter, E.; Batzill, M. Why is anatase a better photocatalyst than rutile?—Model studies on epitaxial TiO_2 films. *Sci. Rep.* **2014**, *4*, 4043. [CrossRef] [PubMed]
7. Sang, Y.; Liu, H.; Umar, A. Photocatalysis from UV/Vis to Near-Infrared Light: Towards Full Solar-Light Spectrum Activity. *Chemcatchem* **2015**, *7*, 559–573. [CrossRef]
8. Szabó, T.; Veres, Á.; Cho, E.; Khim, J.; Varga, N.; Dékány, I. Photocatalyst separation from aqueous dispersion using graphene oxide/TiO_2 nanocomposites. *Colloids Surf. A Physicochem. Eng. Asp.* **2013**, *433*, 230–239. [CrossRef]
9. Wang, C.M.; Mallouk, T.E. Wide-range tuning of the titanium dioxide flat-band potential by adsorption of fluoride and hydrofluoric acid. *J. Phys. Chem.* **1990**, *94*, 4276–4280. [CrossRef]
10. Ibrahim, H.H.; Mohamed, A.A.; Ibrahim, I.A. Electronic and optical properties of mono and co-doped anatase TiO_2: First principles calculations. *Mater. Chem. Phys.* **2020**, *252*, 123285. [CrossRef]
11. Chen, Y.; Li, A.; Fu, X.; Peng, Z. Electrospinning-based (N,F)-co-doped TiO_2-δ nanofibers: An excellent photocatalyst for degrading organic dyes and heavy metal ions under visible light. *Mater. Chem. Phys.* **2022**, *291*, 126672. [CrossRef]
12. Bai, J.; Zhou, B.; Li, L.; Liu, Y.; Zheng, Q.; Shao, J.; Zhu, X.; Cai, W.; Liao, J.; Zou, L. The formation mechanism of titania nanotube arrays in hydrofluoric acid electrolyte. *J. Mater. Sci.* **2008**, *43*, 1880–1884. [CrossRef]
13. Liu, S.; Yu, J.; Jaroniec, M. Anatase TiO_2 with Dominant High-Energy {001} Facets: Synthesis, Properties, and Applications. *Chem. Mater.* **2011**, *23*, 4085–4093. [CrossRef]
14. Todorova, N.; Giannakopoulou, T.; Romanos, G.; Vaimakis, T.; Yu, J.; Trapalis, C. Preparation of Fluorine-Doped TiO_2 Photocatalysts with Controlled Crystalline Structure. *Int. J. Photoenergy* **2008**, *2008*, 534038. [CrossRef]
15. Tang, J.; Quan, H.; Ye, J. Photocatalytic Properties and Photoinduced Hydrophilicity of Surface-Fluorinated TiO_2. *Chem. Mater.* **2006**, *19*, 116–122. [CrossRef]
16. Li, S.; Hennigan, J.M.; Dixon, D.A.; Peterson, K.A. Accurate Thermochemistry for Transition Metal Oxide Clusters. *J. Phys. Chem. A* **2009**, *113*, 7861–7877. [CrossRef] [PubMed]
17. Buddee, S.; Wongnawa, S.; Sirimahachai, U.; Puetpaibool, W. Recyclable UV and visible light photocatalytically active amorphous TiO_2 doped with M (III) ions (M = Cr and Fe). *Mater. Chem. Phys.* **2011**, *126*, 167–177. [CrossRef]
18. Štengl, V.; Bakardjieva, S.; Murafa, N. Preparation and photocatalytic activity of rare earth doped TiO_2 nanoparticles. *Mater. Chem. Phys.* **2009**, *114*, 217–226. [CrossRef]
19. Huang, D.; Ying, F.; Chen, S.; Zhou, C.; Su, P.; Wu, W. Metal–Ligand Bonds in Rare Earth Metal–Biphenyl Complexes. *Inorg. Chem.* **2022**, *61*, 8135–8143. [CrossRef]
20. Ji, T.; Liu, Y.; Zhao, H.; Du, H.; Sun, J.; Ge, G. Preparation and up-conversion fluorescence of rare earth (Er^{3+} or Yb^{3+}/Er^{3+})-doped TiO_2 nanobelts. *J. Solid State Chem.* **2010**, *183*, 584–589. [CrossRef]
21. Cho, H.; Joo, H.; Kim, H.; Kim, J.-E.; Kang, K.-S.; Jung, H.; Yoon, J. Enhanced Photoelectrochemical Activity of TiO_2 Nanotubes Decorated with Lanthanide Ions for Hydrogen Production. *Catalysts* **2022**, *12*, 866. [CrossRef]
22. Kataura, H.; Kumazawa, Y.; Maniwa, Y.; Umezu, I.; Suzuki, S.; Ohtsuka, Y.; Achiba, Y. Optical properties of single-wall carbon nanotubes. *Synth. Met.* **1999**, *103*, 2555–2558. [CrossRef]
23. Yen, C.-Y.; Lin, Y.-F.; Hung, C.-H.; Tseng, Y.-H.; Ma, C.-C.M.; Chang, M.-C.; Shao, H. The effects of synthesis procedures on the morphology and photocatalytic activity of multi-walled carbon nanotubes/TiO_2 nanocomposites. *Nanotechnology* **2008**, *19*, 045604. [CrossRef] [PubMed]
24. Zhao, C.; Guo, J.; Yu, C.; Zhang, Z.; Sun, Z.; Piao, X. Fabrication of CNTs-Ag-TiO_2 ternary structure for enhancing visible light photocatalytic degradation of organic dye pollutant. *Mater. Chem. Phys.* **2020**, *248*, 122873. [CrossRef]

25. Lam, S.-M.; Sin, J.-C.; Mohamed, A.R. Parameter effect on photocatalytic degradation of phenol using TiO_2-P25/activated carbon (AC). *Korean J. Chem. Eng.* **2010**, *27*, 1109–1116. [CrossRef]
26. Jiang, T.; Zhang, L.; Ji, M.; Wang, Q.; Zhao, Q.; Fu, X.; Yin, H. Carbon nanotubes/TiO_2 nanotubes composite photocatalysts for efficient degradation of methyl orange dye. *Particuology* **2013**, *11*, 737–742. [CrossRef]
27. Yang, H.M.; Park, S.-J. Effect of incorporation of multiwalled carbon nanotubes on photodegradation efficiency of mesoporous anatase TiO_2 spheres. *Mater. Chem. Phys.* **2017**, *186*, 261–270. [CrossRef]
28. Wang, H.; Dong, S.; Chang, Y.; Faria, J.L. Enhancing the photocatalytic properties of TiO_2 by coupling with carbon nanotubes and supporting gold. *J. Hazard. Mater.* **2012**, *235–236*, 230–236. [CrossRef]
29. Zhao, D.; Yang, X.; Chen, C.; Wang, X. Enhanced photocatalytic degradation of methylene blue on multiwalled carbon nanotubes–TiO_2. *J. Colloid Interface Sci.* **2013**, *398*, 234–239. [CrossRef]
30. Kuvarega, A.T.; Krause, R.W.M.; Mamba, B.B. Nitrogen/Palladium-Codoped TiO_2 for Efficient Visible Light Photocatalytic Dye Degradation. *J. Phys. Chem. C* **2011**, *115*, 22110–22120. [CrossRef]
31. Mamba, G.; Mamo, M.A.; Mbianda, X.Y.; Mishra, A.K. Nd,N,S-TiO_2 Decorated on Reduced Graphene Oxide for a Visible Light Active Photocatalyst for Dye Degradation: Comparison to Its MWCNT/Nd,N,S-TiO_2 Analogue. *Ind. Eng. Chem. Res.* **2014**, *53*, 14329–14338. [CrossRef]
32. Mamba, G.; Mbianda, X.Y.; Mishra, A.K. Gadolinium nanoparticle-decorated multiwalled carbon nanotube/titania nanocomposites for degradation of methylene blue in water under simulated solar light. *Environ. Sci. Pollut. Res.* **2014**, *21*, 5597–5609. [CrossRef] [PubMed]
33. Nguyen, K.C.; Ngoc, M.P.; Van Nguyen, M. Enhanced photocatalytic activity of nanohybrids TiO_2 /CNTs materials. *Mater. Lett.* **2016**, *165*, 247–251. [CrossRef]
34. Chen, J.S.; Tan, Y.L.; Li, C.M.; Cheah, Y.L.; Luan, D.; Madhavi, S.; Boey, F.Y.C.; Archer, L.A.; Lou, X.W. Constructing Hierarchical Spheres from Large Ultrathin Anatase TiO_2 Nanosheets with Nearly 100% Exposed (001) Facets for Fast Reversible Lithium Storage. *J. Am. Chem. Soc.* **2010**, *132*, 6124–6130. [CrossRef] [PubMed]
35. Shanmugharaj, A.; Bae, J.; Lee, K.Y.; Noh, W.H.; Lee, S.H.; Ryu, S.H. Physical and chemical characteristics of multiwalled carbon nanotubes functionalized with aminosilane and its influence on the properties of natural rubber composites. *Compos. Sci. Technol.* **2007**, *67*, 1813–1822. [CrossRef]
36. Kuvarega, A.; Krause, R.W.M.; Mamba, B. Multiwalled carbon nanotubes decorated with nitrogen, palladium co-doped TiO_2 (MWCNT/N, Pd co-doped TiO_2) for visible light photocatalytic degradation of Eosin Yellow in water. *J. Nanopart. Res.* **2012**, *14*, 776. [CrossRef]
37. Koli, V.B.; Dhodamani, A.G.; Delekar, S.D.; Pawar, S.H. In situ sol-gel synthesis of anatase TiO_2 -MWCNTs nanocomposites and their photocatalytic applications. *J. Photochem. Photobiol. A Chem.* **2017**, *333*, 40–48. [CrossRef]
38. Mamba, G.; Mbianda, X.; Mishra, A. Enhanced visible light photocatalytic degradation of eriochrome black T and eosin blue shade in water using tridoped titania decorated on SWCNTs and MWCNTs: Effect of the type of carbon nanotube incorporated. *Mater. Chem. Phys.* **2015**, *149–150*, 734–742. [CrossRef]
39. Popov, V.N. Carbon nanotubes: Properties and application. *Mater. Sci. Eng. R Rep.* **2004**, *43*, 61–102. [CrossRef]
40. Xu, Y.-J.; Zhuang, Y.; Fu, X. New Insight for Enhanced Photocatalytic Activity of TiO_2 by Doping Carbon Nanotubes: A Case Study on Degradation of Benzene and Methyl Orange. *J. Phys. Chem. C* **2010**, *114*, 2669–2676. [CrossRef]
41. Wu, C.-H.; Kuo, C.-Y.; Chen, S.-T. Synergistic effects between TiO_2 and carbon nanotubes (CNTs) in a TiO_2/CNTs system under visible light irradiation. *Environ. Technol.* **2013**, *34*, 2513–2519. [CrossRef] [PubMed]
42. Teixeira, S.; Martins, P.M.; Lanceros-Mendez, S.; Kühn, K.; Cuniberti, G. Reusability of photocatalytic TiO_2 and ZnO nanoparticles immobilized in poly(vinylidene difluoride)-co-trifluoroethylene. *Appl. Surf. Sci.* **2016**, *384*, 497–504. [CrossRef]
43. Tian, L.; Ye, L.; Deng, K.; Zan, L. TiO_2/carbon nanotube hybrid nanostructures: Solvothermal synthesis and their visible light photocatalytic activity. *J. Solid State Chem.* **2011**, *184*, 1465–1471. [CrossRef]
44. Hamadanian, M.; Jabbari, V.; Shamshiri, M.; Asad, M.; Mutlay, I. Preparation of novel hetero-nanostructures and high efficient visible light-active photocatalyst using incorporation of CNT as an electron-transfer channel into the support TiO_2 and PbS. *J. Taiwan Inst. Chem. Eng.* **2013**, *44*, 748–757. [CrossRef]
45. Du, Y.; Niu, X.; Li, W.; Liu, J.; Li, J. Synthesis of High-Energy Faceted TiO_2 Nanocrystals with Enhanced Photocatalytic Performance for the Removal of Methyl Orange. *Catalysts* **2022**, *12*, 1534. [CrossRef]
46. Mamba, G.; Mbianda, X.Y.; Mishra, A.K. Photocatalytic degradation of the diazo dye naphthol blue black in water using MWCNT/Gd,N,S-TiO_2 nanocomposites under simulated solar light. *J. Environ. Sci.* **2015**, *33*, 219–228. [CrossRef]
47. Zhou, H.; Qiu, Y.; Yang, C.; Zang, J.; Song, Z.; Yang, T.; Li, J.; Fan, Y.; Dang, F.; Wang, W. Efficient Degradation of Congo Red in Water by UV-Vis Driven $CoMoO_4$/PDS Photo-Fenton System. *Molecules* **2022**, *27*, 8642. [CrossRef]
48. Solís, M.; Solís, A.; Pérez, H.I.; Manjarrez, N.; Flores, M. Microbial decolouration of azo dyes: A review. *Process. Biochem.* **2012**, *47*, 1723–1748. [CrossRef]
49. Wang, W.; Serp, P.; Kalck, P.; Faria, J.L. Visible light photodegradation of phenol on MWNT-TiO_2 composite catalysts prepared by a modified sol–gel method. *J. Mol. Catal. A Chem.* **2005**, *235*, 194–199. [CrossRef]
50. Leary, R.; Westwood, A. Carbonaceous nanomaterials for the enhancement of TiO_2 photocatalysis. *Carbon* **2011**, *49*, 741–772. [CrossRef]

51. Czech, B.; Buda, W. Photocatalytic treatment of pharmaceutical wastewater using new multiwall-carbon nanotubes/TiO_2/SiO_2 nanocomposites. *Environ. Res.* **2015**, *137*, 176–184. [CrossRef] [PubMed]
52. Wu, C.-Y.; Tu, K.-J.; Deng, J.-P.; Lo, Y.-S.; Wu, C.-H. Markedly Enhanced Surface Hydroxyl Groups of TiO_2 Nanoparticles with Superior Water-Dispersibility for Photocatalysis. *Materials* **2017**, *10*, 566. [CrossRef]
53. Sun, K.; Vasudev, M.; Jung, H.-S.; Yang, J.; Kar, A.; Li, Y.; Reinhardt, K.; Snee, P.; Stroscio, M.A.; Dutta, M. Applications of colloidal quantum dots. *Microelectron. J.* **2009**, *40*, 644–649. [CrossRef]
54. Hunge, Y.M.; Yadav, A.A.; Kang, S.-W. Photocatalytic Degradation of Eriochrome Black-T Using $BaWO_4$/MoS_2 Composite. *Catalysts* **2022**, *12*, 1290. [CrossRef]
55. Hisaindee, S.; Meetani, M.; Rauf, M. Application of LC-MS to the analysis of advanced oxidation process (AOP) degradation of dye products and reaction mechanisms. *TrAC Trends Anal. Chem.* **2013**, *49*, 31–44. [CrossRef]
56. Larkin, P. General outline and strategies for IR and Raman spectral interpretation. In *Infrared and Raman Spectroscopy: Principles and Spectral Interpretation*, 1st ed.; Larkin, P., Ed.; Elsevier: London, UK, 2011; pp. 117–133.
57. Skalska, K.; Malankowska, A.; Balcerzak, J.; Gazda, M.; Nowaczyk, G.; Jurga, S.; Zaleska-Medynska, A. NO_x Photooxidation over Different Noble Metals Modified TiO_2. *Catalysts* **2022**, *12*, 857. [CrossRef]
58. Wang, Y.; Yu, Q.; Xue, L.; Yu, Q.; Zhu, X. Selective Synthesis of 1,4-Dioxane from Oxirane Dimerization over ZrO_2/TiO_2 Catalyst at Low Temperature. *Catalysts* **2022**, *12*, 832. [CrossRef]
59. Dalhatou, S.; Sali, M.; Tetteh, S.; Boubakari, A.; Talami, B.; Zeghioud, H.; Kane, A.; El Jery, A.; Assadi, A.A.; Obada, D.O. Sorbent and Photocatalytic Potentials of Local Clays for the Removal of Organic Xenobiotic: Case of Crystal Violet. *Catalysts* **2022**, *12*, 899. [CrossRef]
60. Hunge, Y.; Yadav, A.; Dhodamani, A.; Suzuki, N.; Terashima, C.; Fujishima, A.; Mathe, V. Enhanced photocatalytic performance of ultrasound treated GO/TiO_2 composite for photocatalytic degradation of salicylic acid under sunlight illumination. *Ultrason. Sonochem.* **2020**, *61*, 104849. [CrossRef] [PubMed]
61. Sun, M.; Senthil, R.A.; Pan, J.; Osman, S.; Khan, A. A Facile Synthesis of Visible-Light Driven Rod-on-Rod like α-FeOOH/α-AgVO3 Nanocomposite as Greatly Enhanced Photocatalyst for Degradation of Rhodamine B. *Catalysts* **2018**, *8*, 392. [CrossRef]
62. Osman, N.; Sulaiman, S.; Muhamad, E.; Mukhair, H.; Tan, S.; Abdullah, A. Synthesis of an Ag_3PO_4/Nb_2O_5 Photocatalyst for the Degradation of Dye. *Catalysts* **2021**, *11*, 458. [CrossRef]
63. Amano, F.; Yamamoto, A.; Kumagai, J. Highly Active Rutile TiO_2 for Photocatalysis under Violet Light Irradiation at 405 nm. *Catalysts* **2022**, *12*, 1079. [CrossRef]
64. Sakar, M.; Prakash, R.M.; Do, T.-O. Insights into the TiO_2-Based Photocatalytic Systems and Their Mechanisms. *Catalysts* **2019**, *9*, 680. [CrossRef]
65. Jia, L.; Li, F.; Yang, C.; Yang, X.; Kou, B.; Xing, Y.; Peng, J.; Ni, G.; Cao, Z.; Zhang, S.; et al. Direct Z-Scheme Heterojunction α-MnO_2/BiOI with Oxygen-Rich Vacancies Enhanced Photoelectrocatalytic Degradation of Organic Pollutants under Visible Light. *Catalysts* **2022**, *12*, 1596. [CrossRef]

Disclaimer/Publisher's Note: The statements, opinions and data contained in all publications are solely those of the individual author(s) and contributor(s) and not of MDPI and/or the editor(s). MDPI and/or the editor(s) disclaim responsibility for any injury to people or property resulting from any ideas, methods, instructions or products referred to in the content.